

# CHARACTERIZATION OF DUAL-BAND CIRCULARLY POLARIZED ACTIVE ELECTRONICALLY SCANNED ARRAYS (AESA) USING ELECTRO-OPTIC FIELD PROBES

Kazem Sabet, Richard Darragh, Ali Sabet and Sean Hatch

EMAG Technologies Inc.  
775 Technology Drive, Suite 300  
Ann Arbor, MI 48108, USA  
[ksabet@emagtech.com](mailto:ksabet@emagtech.com)

**Abstract**—Electro-optic (EO) probes provide an ultra-wideband, high-resolution, non-invasive technique for polarimetric near-field scanning of antennas and phased arrays. Unlike conventional near field scanning system which typically involve metallic components, the small footprint all-dielectric EO probes can get extremely close to an RF device under test (DUT) without perturbing its fields. In this paper, we discuss and present measurement results for EO field mapping of a dual-band circularly polarized active phased array that operates at two different S and C bands: 2.1GHz and 4.8GHz. The array uses probe-fed, cross-shaped, patch antenna elements at the S-band and dual-slot-fed rectangular patch elements at the C-band. At each frequency band, the array works both as transmitting and receiving antennas. The antenna elements have been configured as scalable array tiles that are arranged together to create large apertures.

## I. INTRODUCTION

The design of active electronically steered arrays (AESA) is a challenging, time-consuming and costly endeavor. The design process becomes much more sophisticated in the case of dual-band circularly polarized active phased arrays, in which CP radiating elements at two different frequency bands occupy a common shared aperture. A design process that takes into account various inter-element and intra-element coupling effects at different frequency bands currently relies solely on computer simulations.

Compact near-field test ranges have been developed and exploited to characterize antenna systems [1]-[2]. Conventional near-field ranges measure the near-zone fields radiated by the antenna under test (AUT) either on a cylindrical or spherical surface surrounding the device. The conventional near-field scanning systems have serious limitations for quantifying the array coupling effects mainly due to the invasive nature of their metallic probes. These probes indeed act as receiving antennas and have to be placed far enough from the AUT to avoid perturbing the latter's near fields. A more recent development is reported in [3] which uses a photonic probe for near-field measurement that can be placed closer to the AUT up to a wavelength away. The proposed photonic probe is indeed a printed metallic dipole array deposited on an optical substrate.

During the last two decades, the researchers at the University of Michigan and EMAG Technologies Inc. have developed a unique novel technology for near field mapping using electro-optic (EO) crystals [4]-[5]. Unlike the photonic antenna probes

of [3], the EO probes are completely made of non-metallic parts. As a results, they are non-invasive and virtually transparent to the RF at frequencies up to 20GHz. This ultra-wideband, high-resolution technique uses the linear Pockels effect in certain electro-optic crystals to modulate the polarization state of a propagating optical beam with the RF electric field penetrating and present inside the crystal. The far field radiation patterns of the AUT can then be estimated accurately from a knowledge of near-field scan maps.

In this paper, we will present near-field and far-field measurement data for a dual-band circularly polarized active phased array that operates at two different S and C bands: 2.1GHz and 4.8GHz. The array uses probe-fed, cross-shaped, patch antenna elements at the S-band and dual-slot-fed rectangular patch elements at the C-band. At each frequency band, the AESA works both as transmitting and receiving antennas using T/R switches. The antenna elements have been configured as scalable array tiles that can be combined together to create larger apertures. Each tile contains all the active devices such as power amplifiers (PA), low-noise amplifiers (LNA), phase shifters and T/R switches. A carrier board is used for the purpose of tiling, which also provides thermal management infrastructure as well as the digital beam control system.

In the following sections, first we briefly describe the EO field probe system. Next, we establish the theoretical foundation for the computation of far-field characteristics based on the near-field maps. Finally, we present near-field and far-field measurement data for a single dual-band AESA tile as well as a larger aperture made up of four side-by-side AESA tiles.

## II. THE ELECTRO-OPTIC FIELD PROBE

Imposing an external electric field on an electro-optic (EO) crystal induces a change in its refractive index, which then leads to a change in the polarization of an optical beam that passes through the EO crystal (linear birefringence) as shown in Figure 1. This in turn produces a measurable change in the optical intensity of the beam at a polarization analyzer. The EO field probes are constructed from extremely small EO crystals mounted at the tip of an optical fiber. Figure 2 shows the photograph of a fiber-coupled EO field probe placed at a very low height above the surface of a dual-band AESA tile. The probe holder fixture is mounted on a computer-controlled XY translation stage that can scan the surface of the antenna tile.

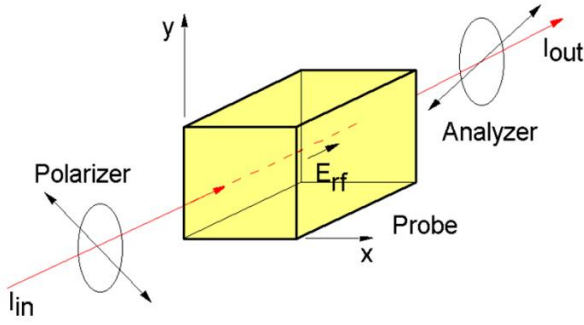


Figure 1: An optical beam propagating through an EO crystal and experiencing polarization change due to Pockels' effect.

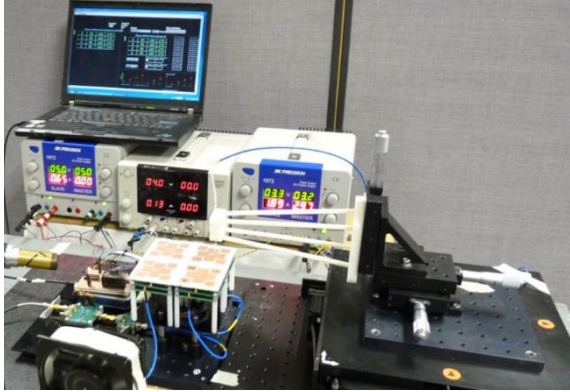
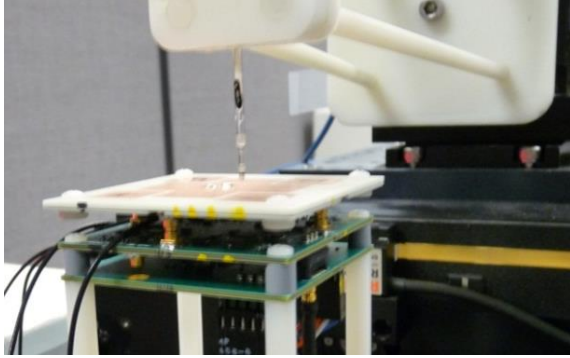


Figure 2: An EO probe mounted on an XY translation stage scanning the near fields of a dual-band AESA antenna.

The EO probe is connected via a polarization maintaining optical fiber to the optical mainframe of the NeoScan system [8], a turnkey electric field measurement system. This system can measure the amplitude and phase of the electric field simultaneously with a sub-millimeter resolution. The optically detected RF signal is down-converted to 100MHz and processed through a lock-in amplifier that is synchronized (phase-locked) with the signal generator or frequency synthesizer that feeds the AUT. The combination of the small probe size and non-metallic, all-dielectric parts leads to the ultimate RF non-invasiveness. Some of the key features of our field probe systems include:

- Broad measurement bandwidth (>20GHz) using the same optical probes

- High spatial resolution driven by the laser beam spot size (finer than  $100 \mu\text{m}^2$ )
- Simultaneous amplitude and phase measurement
- Vectorial field measurement with very cross-polarization suppression better than 20dB

The EO field probes provide accurate multi-dimensional signal flow maps of RF, microwave and millimeter wave devices and circuits. Near-field maps of this kind can be very useful for investigation of inter-element coupling effects in antenna array structures, phase calibration of their aperture, or many other diagnostic applications. The near-field maps at slightly higher planes, where the device's evanescent, reactive fields decay sufficiently, can effectively be used to compute the far field radiation patterns of the AUT.

### III. THEORETICAL FOUNDATION FOR FAR FIELD MEASUREMENT

According to the equivalence principle in electromagnetics, if the tangential electric and magnetic field components are known on the surface of a closed surface like a box enclosing a radiating system, then one can determine the electric and magnetic fields everywhere outside that surface [7]. This applies equally well to the far-zone radiated fields of the structure under test. Such a closed surface is typically known as a Huygens surface. According to the equivalence theorem, one can define equivalent electric and magnetic surface current on the Huygens surface in the following manner:

$$\begin{aligned} \mathbf{J}_s(\mathbf{r}) &= \hat{\mathbf{n}} \times \mathbf{H}(\mathbf{r}) \\ \mathbf{M}_s(\mathbf{r}) &= -\hat{\mathbf{n}} \times \mathbf{E}(\mathbf{r}) \end{aligned} \quad (1)$$

where  $\hat{\mathbf{n}}$  is the unit outward normal vector on the Huygens surface. The radiated electric and magnetic fields by these equivalent sources in the free space are then given by:

$$\mathbf{E}(\mathbf{r}) = \mathbf{E}^{\text{inc}}(\mathbf{r}) - jk_0 Z_0 \iint_{S_j} \left\{ \begin{aligned} &\left[ 1 - \frac{j}{k_0 R} - \frac{1}{(k_0 R)^2} \right] \mathbf{J}(\mathbf{r}') \\ &\left[ 1 - \frac{3j}{k_0 R} - \frac{3}{(k_0 R)^2} \right] (\hat{\mathbf{R}} \cdot \mathbf{J}(\mathbf{r}')) \hat{\mathbf{R}} \end{aligned} \right\} \frac{e^{-jk_0 R}}{4\pi R} ds' \quad (2)$$

$$+ jk_0 \iint_{S_M} \left[ 1 - \frac{j}{k_0 R} \right] (\hat{\mathbf{R}} \times \mathbf{M}(\mathbf{r}')) \frac{e^{-jk_0 R}}{4\pi R} ds'$$

$$\mathbf{H}(\mathbf{r}) = \mathbf{H}^{\text{inc}}(\mathbf{r}) - jk_0 Y_0 \iint_{S_M} \left\{ \begin{aligned} &\left[ 1 - \frac{j}{k_0 R} - \frac{1}{(k_0 R)^2} \right] \mathbf{M}(\mathbf{r}') \\ &\left[ 1 - \frac{3j}{k_0 R} - \frac{3}{(k_0 R)^2} \right] (\hat{\mathbf{R}} \cdot \mathbf{M}(\mathbf{r}')) \hat{\mathbf{R}} \end{aligned} \right\} \frac{e^{-jk_0 R}}{4\pi R} ds' \quad (3)$$

$$- jk_0 \iint_{S_j} \left[ 1 - \frac{j}{k_0 R} \right] (\hat{\mathbf{R}} \times \mathbf{J}(\mathbf{r}')) \frac{e^{-jk_0 R}}{4\pi R} ds'$$

where  $\mathbf{r}$  and  $\mathbf{r}'$  are the position vectors at the observation and source points, respectively, and  $R = |\mathbf{r} - \mathbf{r}'|$ . In the above equations,  $\mathbf{E}^{\text{inc}}$  and  $\mathbf{H}^{\text{inc}}$  account for any impressed or incident electric and magnetic fields besides the fields radiated by the

equivalent surface electric and magnetic currents  $\mathbf{J}$  and  $\mathbf{M}$ . In the Fraunhofer region around the radiating structure, the far-zone fields can be approximated by:

$$\mathbf{E}^{\text{fr}}(\mathbf{r}) = \frac{jk_0}{4\pi} \frac{e^{-jk_0 r}}{r} \left\{ \begin{aligned} &Z_0 \hat{\mathbf{r}} \times \hat{\mathbf{r}} \times \iint_{S_J} \mathbf{J}(\mathbf{r}') e^{-jk_0 \hat{\mathbf{r}} \cdot \mathbf{r}'} ds' \\ &+ \hat{\mathbf{r}} \times \iint_{S_M} \mathbf{M}(\mathbf{r}') e^{-jk_0 \hat{\mathbf{r}} \cdot \mathbf{r}'} ds' \end{aligned} \right\} \quad (4)$$

$$\mathbf{H}^{\text{fr}}(\mathbf{r}) = \frac{1}{Z_0} \hat{\mathbf{r}} \times \mathbf{E}^{\text{fr}}(\mathbf{r})$$

In the limiting case, a closed Huygens surface may consist of a plane placed slightly above the surface of an antenna and laterally extending to the infinity. This unbounded plane together with a hemisphere of infinite radius in the lower half-space constitutes a closed Huygens surface, completely encircling the radiating structure under test. Most practical antennas and array systems have highly evanescent near-zone fields at the surface of the radiator, which fade away very quickly in the lateral directions. This amounts to vanishing tangential E- and H-field components everywhere on the infinite Huygens plane except in the area directly above the antenna. This area will constitute the scanning plane where the EO field probe measures the tangential field components.

#### IV. DUAL-BAND CIRCULARLY POLARIZED ACTIVE PHASED ARRAY FOR NANOSATELLITE COMMUNICATIONS

A dual-band circularly polarized (CP) active phased array has been developed for nanosatellite communications. The AESA system operates as both transmitter and receiver at two different frequency bands: 2.1GHz (S-band) and 4.8GHz (C-band). The S-band CP radiating element consists of a probe-fed, cross-shaped patch with two orthogonal probe feed located close to the center of the cross. The C-band CP radiating element consists of a dual-slot-fed rectangular patch with two orthogonal edge slots located underneath the patch and excited by two microstrip lines, which are terminated in open quarter-wave stubs and are connected to the in-phase and quadrature ports of a hybrid branchline coupler. Each AESA tile contains one S-band cross patch and four satellite C-band rectangular patches with a total surface area of 65mm  $\times$  65mm.

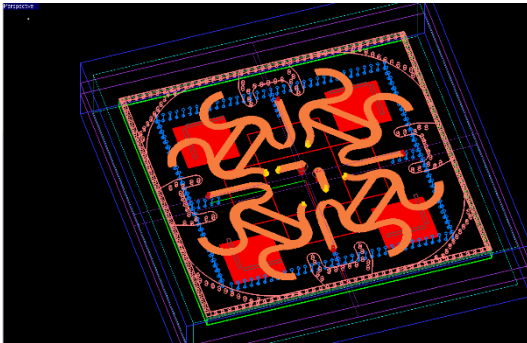


Figure 3: The unit cell of the dual-band circularly polarized AESA tile.

The tile consists of three vertically stacked printed circuit boards: the antenna board at the top, the C-band transceiver board sandwiched in the middle and the S-band transceiver

board at the bottom. Miniature SMPM connectors are used to interconnect the boards. The entire design was developed using EM.Cube's FDTD Module [9]. Figure 3 shows the layout of the antenna board of the unit cell tile. Figures 4 and 5 show the computed 3D radiation pattern of an aperture consisting of four AESA tiles at 2.1GHz and 4.8GHz, respectively. In the latter case, the beam of the C-band array has been steered at an elevation angle of 22° and an azimuth angle of 180°.

In each AESA tile, a 90° rotational phase progression is necessary among the four C-band patch elements to achieve circular polarization. The beam steering of the array is accomplished using a USB-controlled LabView interface that reads user supplied elevation and azimuth scan angles and translates them to 6-bit digital phase shift data. Each AESA tile integrates one S-band and four C-band 6-bit digital phase shifter devices within the two stacked transceiver boards. Using a network of T/R switches, the same phase shifters are shared by both transmit and receive chains in each transceiver board.

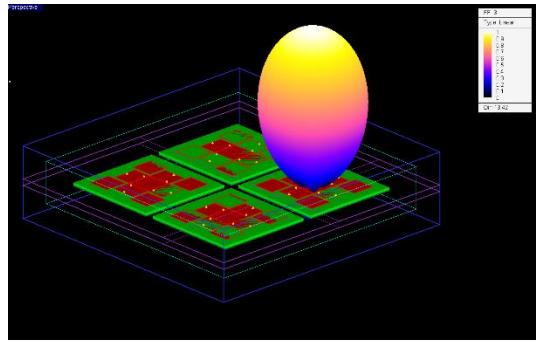


Figure 4: Computed 3D far field radiation pattern of the four-tile dual-band AESA array at 2.1GHz.

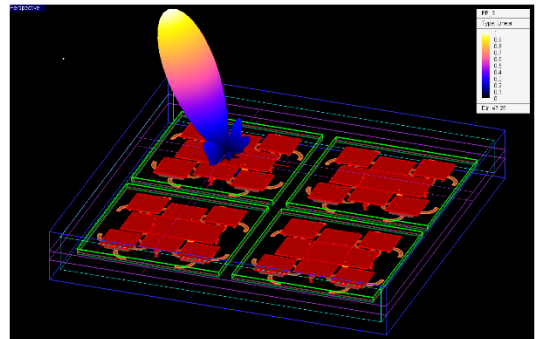


Figure 5: Computed 3D far field radiation pattern of the four-tile dual-band AESA array at 4.8GHz with scan angles  $\theta = -22^\circ$ ,  $\phi = 180^\circ$ .

#### V. MEASUREMENT RESULTS

The dual-band circularly polarized (CP) AESA tile, whose design was described in the previous section, was fabricated and assembled. Four AESA tiles were next combined and arranged using a common carrier board to build a 2 $\times$ 2 S-band CP array and a 4 $\times$ 4 C-band CP array sharing a common aperture with a total surface area of 260mm  $\times$  260mm. Figure 6 shows the 4-tile assembly with the common carrier board and the USAB controller device. Figure 6 shows the 4-tile assembly with the common carrier board and the USAB controller device.

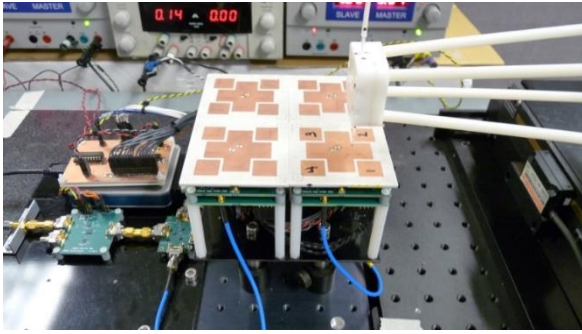


Figure 6: Computed 3D far field radiation pattern of the four-tile dual-band AESA array at 4.8GHz with scan angles  $\theta = -22^\circ$ ,  $\phi = 180^\circ$ .

First, the near-field maps of a single AESA tile were measured at a height of 2mm above the surface of the tile. Figure 7 shows the amplitude and phase maps of the tangential field components measured at 2.1GHz with the S-band cross patch excited. Figure 8 shows the amplitude and phase maps of the tangential field components measured at 4.8GHz with the four C-band patches excited and phase-shifted properly. Next, the amplitude and phase maps of the tangential field components above the surface of a 4-tile AESA assembly were measured at 4.8GHz with 16 C-band patches excited as shown in Figure 9.

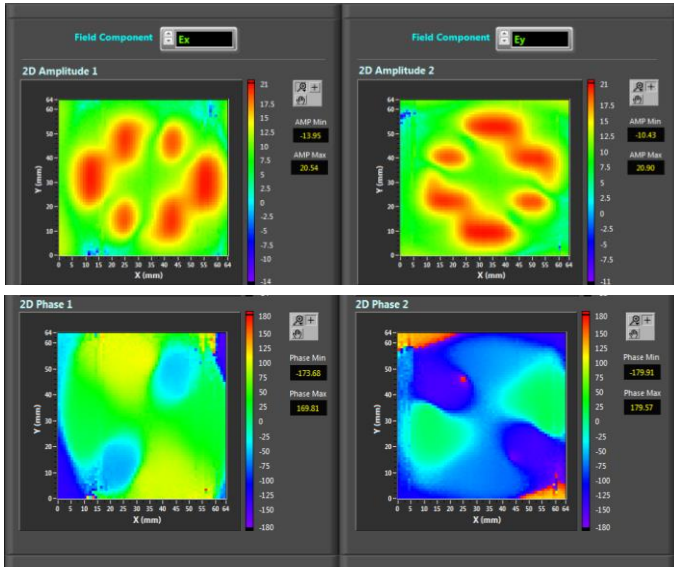


Figure 7: Measured electric field components above the surface of a single dual-band AESA tile at 2.1GHz. Top: Amplitude, Bottom: Phase. Left: Ex, Right: Ey.

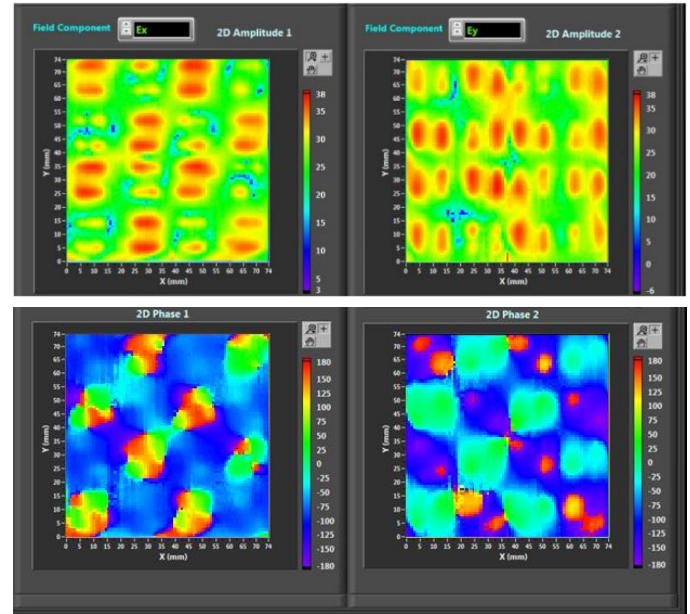


Figure 9: Measured electric field components above the surface of a four-tile dual-band AESA tile at 4.8GHz. Top: Amplitude, Bottom: Phase. Left: Ex, Right: Ey.

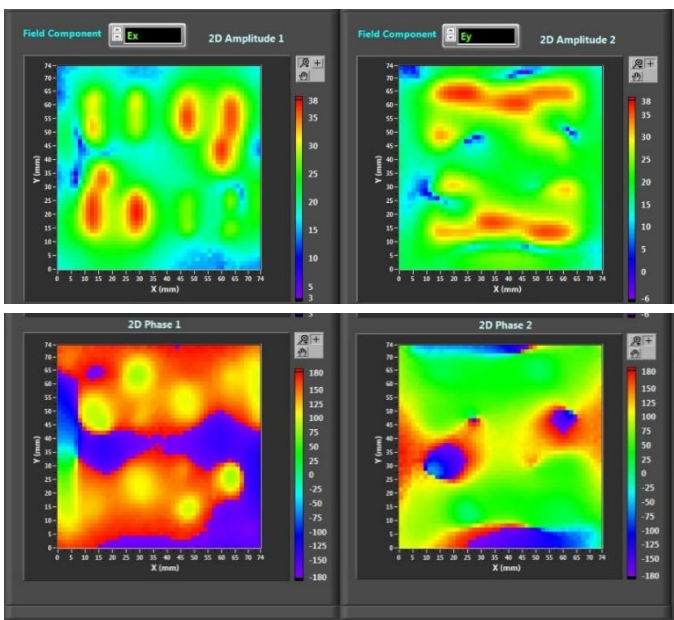


Figure 8: Measured electric field components above the surface of a single dual-band AESA tile at 4.8GHz. Top: Amplitude, Bottom: Phase. Left: Ex, Right: Ey.

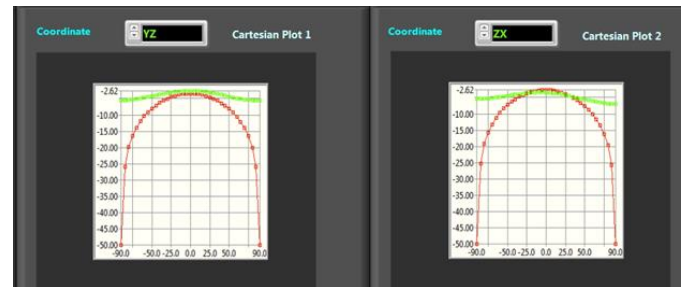


Figure 10: Measured principal-plane radiation patterns of a single dual-band AESA tile at 2.1GHz. Left: YZ plane, Right: ZX plane.



Figure 11: Measured principal-plane radiation patterns of a single dual-band AESA tile at 4.8GHz. Left: YZ plane, Right: ZX plane.

The NeoScan system uses the same near-to-far-field transformation that EM.Cube's FDTD Module utilizes for computation of the far field radiation patterns. The principal-plane radiation patterns of the single AESA tile were thus obtained at 2.1GHz and 4.8 GHz as shown in Figures 10 and 11, respectively. Good circular polarization is observed in both bands. Note that the C-band radiation patterns correspond to a 4-element planar array. Figure 12 shows the principal-plane radiation patterns of the assembly of four AESA tiles (as shown in Figure 6) measured at 4.8 GHz. A satisfactory circular polarization performance is again observed over a fairly large angular field of view.

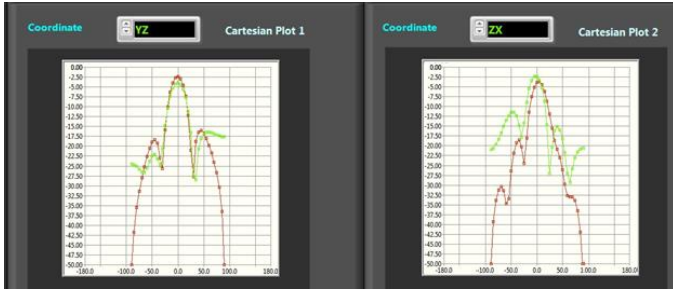


Figure 12: Measured principal-plane radiation patterns of a 4-tile dual-band AESA aperture at 4.8GHz. Left: YZ plane, Right: ZX plane.

The principal-plane radiation patterns of the dual-band CP AESA antenna were further measured at EMAG Technologies' in-house anechoic chamber for additional verification of the NeoScan system's results based on the near-field maps. Figures 13, 14, 15 and 16 show the principal-plane radiation patterns of the 4x4 C-band CP array measured at 4.8GHz in the chamber for different elevation scan angles of 0°, ±15° and ±30°, respectively. Note that positive and negative elevation scan angles in these figures denote those in the azimuth planes  $\phi = 0^\circ$  and  $\phi = 180^\circ$ , respectively.

### CONCLUSION

In this paper, we have used a wideband, non-invasive, electro-optic field probe to measure the near-field maps of a dual-band circularly polarized active phased array for nanosatellite communications. The near-field distribution profiles have been validated with FDTD simulation data. The far field radiation patterns of the AESA antenna were computed based on the near-field maps and were further verified using the measured radiation patterns of the same active array in an anechoic chamber. Additional measurement and simulation data will be presented at the conference.

### REFERENCES

- [1] M. Hirose, S Kurokawa, and K. Komiyama, "Compact spherical near-field measurement system for UWB antennas," IEEE Intl. Symp. Antennas & Propagat. Digest, Washington DC, July 2005, pp. 692-695.
- [2] A. Capozzoli, C. Curcio, G. D'Elia, and A. Liseno, "Phaseless antenna characterization by effective aperture field and data representations," IEEE Trans. On Antennas & Propagat., vol. AP-57, No. 1, January 2009, pp. 215-230.
- [3] A. Capozzoli, C. Curcio, G. D'Elia, A. Liseno, P. Vinetti, M. Ameya, M. Hirose, S Kurokawa, and K. Komiyama, "Photonic probes and advance

- (also phaseless) near-field far-field techniques," IEEE Antennas & Propagat. Mag., Vol. 52, No. 5, October 2010, pp. 232-241.
- [4] A. Yariv and P. Yeh, *Optical Waves in Crystals*, pp. 220-255, John Wiley & Sons, 1984.
- [5] K. Yang, G. David, J-G. Yook, I. Papapolymerou, L.P.B. Katehi, and J.F. Whitaker, "Electrooptic mapping and finite-element modeling of the near-field pattern of a microstrip patch antenna", IEEE Trans. on Microwave Theory & Tech., Vol. 48, No. 2, February 2000, pp. 288-294.
- [6] K. Yang, t. Marshall, M. Forman, J. Hubert, L. Mirth, Z. Popovic, L.P.B. Katehi, and J.F. Whitaker, "Active-amplifier-array diagnostics using high-resolution electrooptic field mapping", IEEE Trans. on Microwave Theory & Tech., Vol. 49, No. 5, May 2001, pp. 849-857.
- [7] C. A. Balanis, *Advanced Engineering Electromagnetics*, 2<sup>nd</sup> Ed., pp. 328-333, John Wiley & Sons, 2012.
- [8] <http://www.emagtech.com/content/innovative-rf-test-solutions>.
- [9] <http://www.emagtech.com/content/emcube>.

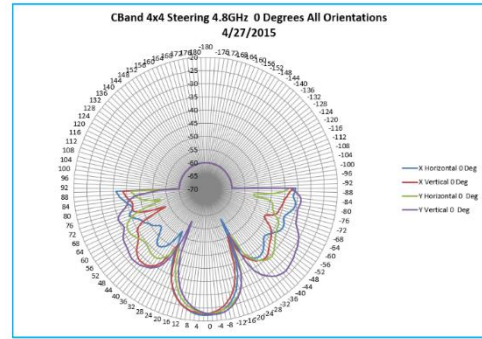


Figure 13: Measured principal-plane radiation patterns of the 4-tile dual-band AESA antenna at 4.8GHz in the anechoic chamber.

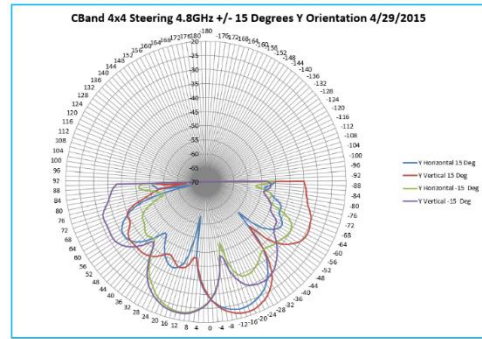


Figure 14: Measured principal-plane radiation patterns of the 4-tile dual-band AESA antenna at 4.8GHz with the array beam steered at an elevation scan angle of ±15°.

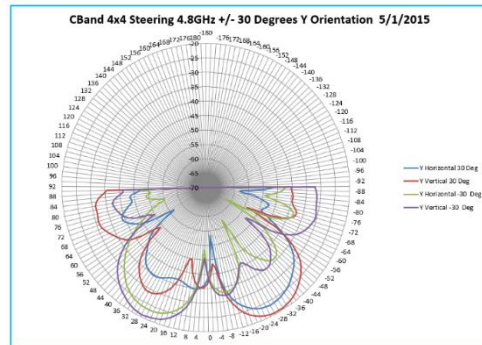


Figure 15: Measured principal-plane radiation patterns of the 4-tile dual-band AESA antenna at 4.8GHz with the array beam steered at an elevation scan angle of ±30°.